Analyzing Full Band Transport in 2D TMDs Using the Monte Carlo Method

Nils Vansteenvoort[1,2], Gautam Gaddemane[1], Bart Sorée[1,2], and Maarten L Van de Put[1]
[1]*Imec, Leuven, Belgium*
[2]*Department of Electrical Engineering, KU Leuven, Leuven, Belgium*

***Abstract*—Theoretical efforts to study transport properties in 2D are either limited to a simplified analytical description with limited applicability beyond the low-field regime or a numerically intensive full-band approach that is prone to discretization errors. In this paper, we describe a first-principles full-band Monte-Carlo method that utilizes full scattering matrix-elements while retaining the benefits of the analytical approach. We apply this method to the study of field-dependent electron transport in monolayer WS$_2$. To show the limits of applicability, we compare our approach to a simplified effective mass method. For the effective mass method, we extract inter- and intra-valley deformation potentials to match closely the scattering rates of the full-band approach.**

I. INTRODUCTION

Semiconducting transition metal dichalcogenides (TMDs), such as MoS$_2$, WS$_2$, and WSe$_2$, have gained significant attention as potential channel materials for next-generation field-effect transistors (FETs) (*1*, *2*). This interest is largely attributed to their ability to suppress short-channel effects at the nanometer-scale (*3*, *4*) and to the enhanced gate control enabled by their intrinsic atomic thickness (*5*). Although recent experimental results have demonstrated promising device metrics, e.g., in a MoS$_2$ nanosheet gate-all-around FET with $L_{SD} = 40$ nm, such as on/off current ratios exceeding 10^9, drive currents up to 451 µA/µm, and subthreshold swings as low as 65 mV/dec (*6*), theoretical modeling remains essential to evaluate the fundamental performance limits and scalability of these materials within advanced device architectures.

As these FETs are expected to operate with gate lengths below 10 nm and drain-source biases approaching 1 V, electric fields as large as 10^6 V/cm can arise along the transport direction (*7*). Under such high-field conditions, models based solely on the effective mass approximation become inadequate, as carriers occupy higher-energy regions of the band structure where this approximation is no longer valid (*8*–*14*). More accurate transport models that incorporate full-band electronic structures and complete scattering matrix elements typically require dense sampling in the first Brillouin zone (FBZ), resulting in impractical computational times and thus, limited scalability (*15*, *16*), or expansion on a suitable global basis set in the Brillouin zone, such as Wannier functions (refs), which require further discretization to access energy-dependent properties such as the density of states (*17*–*20*).

In this work, we present a transport solver based on the semiclassical ensemble Monte Carlo method that incorporates a full-band representation, full scattering matrix elements, and phonon dispersions, all evaluated on a coarse reciprocal space mesh using a novel local and invertible interpolation scheme. This methodology is applied to monolayer WS$_2$, and results are compared with those obtained using an effective mass approximation. Section II provides an overview of the computational approach, Section III presents the transport simulation results, and Section IV concludes the work.

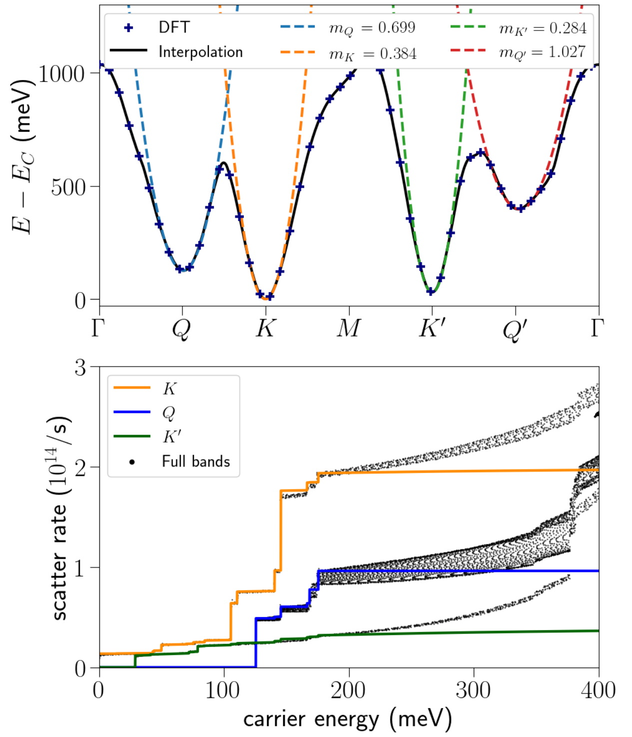

Fig. 1. **Top**: The first band ($n = 1$) of monolayer WS$_2$, the blue crosses give the DFT output, the dashed lines show the EM approximation, and the black line gives the interpolated energy. The second band ($n = 2$) can be obtained by mapping $\boldsymbol{k} \to -\boldsymbol{k}$. **Bottom**: Electron-phonon scatter rates as a function of initial energy, the colors indicate the valley in which the scattering takes place. Scatter rates are calculated using Eq. 7 and summed over all possible transitions. The solid lines give the deformation potential approximation given by Eq. 4 and 5.

II. METHODS

A. Ab-initio material parameter extraction

Electronic band structures are obtained from density functional theory (DFT), while phonon dispersions and the corresponding scattering matrix elements are computed using density functional perturbation theory (DFPT), as implemented in QUANTUM ESPRESSO and PERTURBO (*21*, *22*). Since WS_2 is significantly affected by spin-orbit coupling (SOC), it is included in the calculations. Breaking of time-reversal symmetry due to spin-orbit interaction leads to a splitting of the first conduction band into two. These bands (labeled $n = 1$ and $n = 2$) map into each other by a 60° rotation and each exhibit a 120° degree rotation symmetry. This leads to the emergence of distinct valleys at the K and K' points (see Fig. 1).

B. The analytical ensemble Monte Carlo method

The ensemble Monte Carlo (MC) method is a semiclassical approach used to obtain carrier transport characteristics by statistically solving the Boltzmann transport equation (BTE) (*23*). In this method, the trajectory of an ensemble of carriers is simulated in real and reciprocal space by updating its position $\boldsymbol{r}$ and wavevector $\boldsymbol{k}$ according to:

$$\boldsymbol{r}(t+\delta t) = \boldsymbol{r}(t) + \boldsymbol{v}(t)\delta t + \frac{1}{2}e\boldsymbol{\mathcal{E}}\delta t^2 \tag{1}$$

$$\boldsymbol{k}(t+\delta t) = \boldsymbol{k}(t) + e\boldsymbol{\mathcal{E}}\delta t \tag{2}$$

where δt is the time step, $\boldsymbol{v}$ is the group velocity of the carrier, e is the carrier's charge, and $\boldsymbol{\mathcal{E}}$ is the applied electric field, which is taken as homogeneous through space. This approach yields carrier distributions in both real and reciprocal space, properties of the ensembles, such as the drift velocity and average energy, are calculated by taking an average over time. In this work, we derive analytical expressions for all relevant material properties, including band energies, group velocities, and scattering rates. This approach eliminates the need for a gridded representation, thereby avoiding interpolation-related systematic errors and substantially reducing computational cost. Section II-C introduces the effective mass and deformation potential model for scattering, while Section II-D details the aforementioned interpolation scheme used to obtain full-band quantities.

C. Effective masses and Deformation potentials

An effective mass (EM) model considers a set of valleys, each characterized by its effective mass m^* and energy offset E_0, the dispersion of valley i is given by:

$$E_i(\boldsymbol{k}) = \frac{\hbar^2}{2m_i^*}(\boldsymbol{k} - \boldsymbol{k}_{0i})^2 + E_{0i}, \tag{3}$$

where $\boldsymbol{k}_{0i}$ is the location of the valley in reciprocal space. When including SOC in WS_2 four distinct valleys participate in transport: K, K', Q, and Q' (see Fig. 1). Scatter rates between these valleys are described as by the deformation potential approximation (DPA). The elastic intravalley scattering of the acoustic mode ν is given by

$$S_\nu^i = \frac{2\pi}{\hbar}\frac{D_{i\nu}^2}{Gu_\nu^2}k_b T \rho_i, \tag{4}$$

where G is the mass area density, u_ν sound velocity, $D_{i\nu}$ the deformation potential related to the transition and $\rho_i = m_i^*/(2\pi\hbar^2)$, the density of states of valley i. For inelastic inter- and intervalley transitions from valley i to valley j the strength is given by:

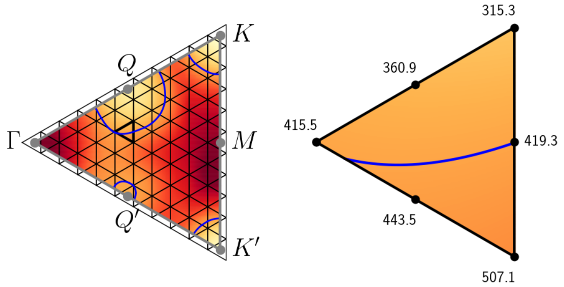

Fig. 2. **Left:** The irreducible wedge of the FBZ of monolayer WS_2, points of interest are labeled with gray dots. The triangular mesh used preform the analytical interpolation is shown in black. The blue line represents an equal energy contour of 420meV, revealing the four valleys also shown in Fig. 1. **Right**: Closer look at one of the mesh elements, the six weights are given by the black dots.

$$S_\nu^{if}(\boldsymbol{k}) = \frac{\pi D_{if\nu}^2}{G\omega_\nu} n_{op} g_f \rho_f \Theta(E_i(\boldsymbol{k}) \pm \hbar\omega_\nu + \Delta_{if}) \tag{5}$$

where g_f is the valley-degeneracy of the final valley, $\hbar\omega_\nu$ the effective phonon energy (taken as constant for each mode), $n_{op} = 1/(-1 + \exp(\hbar\omega_\nu/k_b T))$ the phonon occupancy number and $\Delta_{ij} = E_{0i} - E_{0f}$, the difference in energy offset (*11*). Figure 1 shows the bandstructure and scatter rates calculated with EM and DPA. The potentials were taken so that they closely match the full band scatter rates. Due to the flat density of states arising from 2D EM dispersions, scattering rates exhibit a step-like dependence on energy. The EM and DPA model provides analytical expressions and is straightforward to implement, enabling efficient calculations. However, it does not account for energy regions where the density of states is not flat or for any anisotropy in the scattering rates.

D. Full bands

To accurately capture high-energy transport phenomena relevant under high electric fields, it is essential to account for the full electronic band structure. In this work, we consider conduction bands up to 1 eV above the band edge. To enable this with high efficiency, the band structure is represented using a second-order interpolation scheme defined on a triangular mesh covering the irreducible wedge of the FBZ. Figure 2 illustrates this mesh applied to the first conduction band of monolayer WS_2. Within each triangular element t, the energy dispersion is expressed as a regular two-dimensional quadratic polynomial:

$$E_t(\boldsymbol{k}) = \sum_{i+j\leq 2} c_{tij} k_x^i k_y^j, \tag{6}$$

where the coefficients c_{tij} are based on DFT-calculated band structure data. Due to the intrinsically quadratic nature of the conduction bands, this interpolation achieves high accuracy (root-mean-square error $<$ 1 meV) with a relatively modest dataset (276 points). Near the valley minima, this formulation naturally reduces to a parabolic, effective mass-like description.

The local invertibility of the quadratic dispersion enables analytical selection of $\boldsymbol{k}$-points in the Monte Carlo algorithm, as shown in Fig. 2 for the contour $E_t(k_x, k_y) = 420$ meV. This, together with the smooth nature of the bandstructure, eliminates the need for a finely discretized $\boldsymbol{k}$-space grid and ensures exact energy conservation.

Turing to scattering, the transition rates between electronic states $|n, \boldsymbol{k}\rangle \rightarrow |m, \boldsymbol{k} \pm \boldsymbol{q}\rangle$, where n and m represent band indices and $\boldsymbol{q}$ is the phonon wavevector, are evaluated using Fermi's golden rule:

$$W_\nu^{nm}(\boldsymbol{k}, \boldsymbol{q}) = \frac{2\pi}{\hbar} n_{op} \left| M_\nu^{nm}(\boldsymbol{k}, \boldsymbol{q}) \right|^2 \delta\rho_m(E_n(\boldsymbol{k}) \pm \hbar\omega_\nu(\boldsymbol{q})), \tag{7}$$

where $M_\nu^{nm}(\boldsymbol{k}, \boldsymbol{q})$ denotes the electron-phonon matrix element for phonon mode ν, and $\delta\rho_m(E)$ is the local density of states at energy E in band m. The latter is computed analytically as a line integral over the constant-energy contour $\mathcal{C}_E$:

$$\delta\rho_m(E) = \frac{1}{(2\pi)^2} \int_{\mathcal{C}_E} \frac{\mathrm{d}\ell}{|\nabla_{\boldsymbol{k}} E_m|}. \tag{8}$$

For the matrix elements, we use a linear interpolation approach on the same mesh. Unlike the EM approach, which often leads to step-like artifacts in scattering rates and relies on isotropic approximations, the interpolation-based full-band model supports smoothly varying and anisotropic scattering rates.

To further accelerate the evaluation of the scattering step, we pre-compute element-to-element scattering rates $W_{IF}^{nm\nu}$ where transitions from an initial element I in band n to a final element F in band m via absorption or emission of a phonon of mode ν are assigned fixed rates

$$W_{IF}^{nm\nu} = \max_{\boldsymbol{k}_i \in I} \int_{\boldsymbol{k}_f \in F} W_\nu^{nm}(\boldsymbol{k}_i, \boldsymbol{k}_f - \boldsymbol{k}_i)\, \mathrm{d}^2 k_f, \tag{9}$$

with $\boldsymbol{k}_f = \boldsymbol{k}_i \pm \boldsymbol{q}$. the scatter rates shown in Fig. 1 are then calculated by:

$$S_I^n = \sum_{m\nu} \sum_F W_{IF}^{nm\nu}. \tag{10}$$

Equation 9 over estimates the transition strength by taking the maximum rate, an over-scattering check is implemented in the MC algorithm that rejects a scatter event based on the actual transition rate i.e., Eq. 7 evaluated with the initial k-vector to k-vector that gives the maximal rate as is used to construct Eq. 9. This element-wise formulation provides a higher resolution representation of scattering processes than the valley-to-valley description assumed in the DPA.

III. TRANSPORT RESULTS

The velocity field curves are extracted from MC simulations for both EM and full-band implementations. Figure 3 shows the drift velocity and average energy for a number of electric fields. All results shown are obtained from ensemble MC simulations with 500 particles, 10,000 time steps, and a time step of $\delta t = 5.22 \times 10^{-15}$ s. The first 2,000 data points were neglected to remove the transient response from the initial conditions.

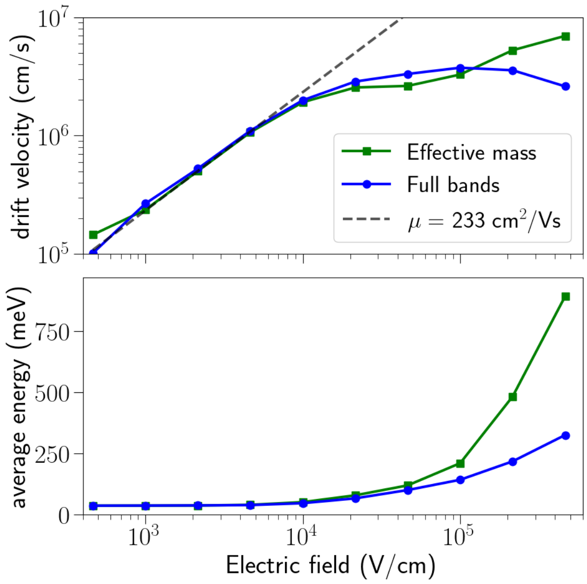

Fig. 3. **Top**: Velocity field curve for intrinsic transport in monolayer WS$_2$ obtained from ensemble MC simulations with 500 particles and 10,000 time steps. **Bottom**: Average carrier energy during a MC simulation at different external electric fields for both the EM and full band implementations.

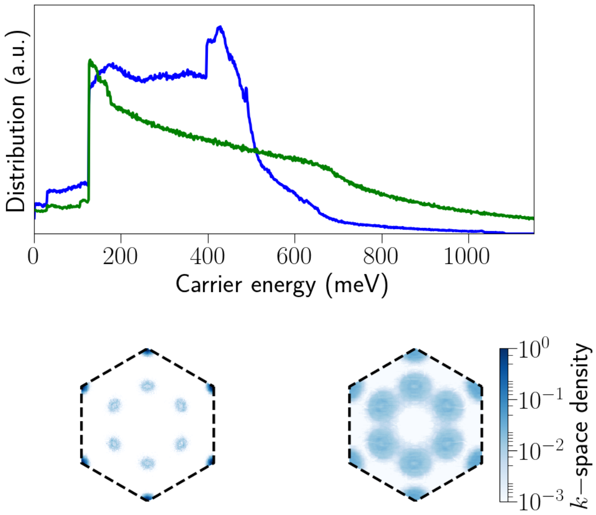

Fig. 4. **Top**: Carrier energy distribution for the high field case (500 kV/cm), EM results are shown in green, full bands in blue. **Bottom**: Reciprocal space distribution on a logarithmic scale for low field (5 kV/cm, left) and high field (500 kV/cm, right) conditions. Both taken from full bands MC simulations.

This method is computationally very efficient. The calculations were performed on a single core (12th Gen Intel® Core™ i7-1265U CPU running at 1.80 GHz, on a laptop) and had an average computation rate of 10^5 iterations per minute.

A. Model comparison

Figure 3 presents a comparison of the field-dependent behavior of both models. In both cases, a linear response is observed at low fields ($\mathcal{E} < 10^4$ V/cm), with a mobility of 233 cm^2/Vs. However, when fields on the order of 10^5 V/cm or higher are applied to the EM model, the average carrier energy begins to deviate from the full-band result. This divergence indicates the breakdown of the EM approximation, as carriers begin to populate energy regions where the underlying assumptions are no longer valid. This effect is further illustrated in Fig. 4, which shows the carrier distributions under high-field conditions. At these fields, the applied electric field pushes carriers into energy ranges where the EM and DPA approximations fail. In contrast, the full-band implementation does not suffer from these limitations and remains well-behaved even for fields exceeding 5×10^5 V/cm.

B. *High field behavior*

In the high-field regime ($\mathcal{E} \approx 10^5$ V/cm), a velocity saturation is observed, as shown in Fig. 3, with a saturation velocity of $v_{\text{sat}} = 3.8 \times 10^6$ cm/s. Beyond this field strength, the system exhibits negative differential mobility (NDM), where the drift velocity decreases with increasing electric field. This phenomenon is similar to the Gunn effect (*24*) seen in bulk semiconductors. NDM occurs when higher electric fields reduce the average mean free path $\langle \lambda \rangle$ of the carrier ensemble. The mean free path λ is defined as:

$$\lambda_n(\boldsymbol{k}) = \frac{|\boldsymbol{v}_n(\boldsymbol{k})|}{\sum_{m\nu} S_\nu^{nm}(\boldsymbol{k})}, \tag{11}$$

where $\boldsymbol{v}_n(\boldsymbol{k}) = \hbar^{-1}\nabla_{\boldsymbol{k}} E_n(\boldsymbol{k})$ is the group velocity.

Figure 5 presents the calculated mean free path across the entire FBZ for both conduction bands of monolayer WS$_2$, alongside a comparison between the EM-DPA and full-band results. A comparison of carrier distributions in k-space from Fig. 4, for electric fields in the linear and NDM regimes, reveals significant differences in the regions of the FBZ contributing to transport. At low fields, transport is dominated by carriers in the K and K' valleys, both exhibiting an average mean free path of approximately 10 nm. In contrast, under high-field conditions, carriers are increasingly redistributed into the Q valley. This valley exhibits a much shorter average mean free path of around 3 nm, thereby reducing the net drift velocity and leading to the onset of NDM.

IV. CONCLUSION

We developed an analytical full-band, full scattering matrix element Monte Carlo transport solver and compared it to an effective mass, deformation potential approach. Our full-band method remains accurate in regimes where the effective mass approximation breaks down while maintaining computational efficiency. This makes it scalable to realistic device geometries.

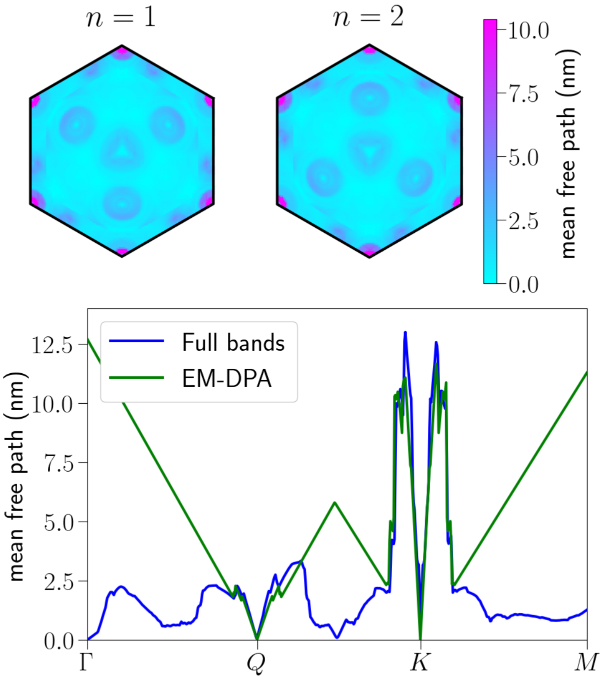

Fig. 5. Mean free path calculated with Eq. 11 **Top**: the first two conduction bands across the FBZ. **Bottom**: Mean free path of the first band ($n = 1$) for both the full bands (blue) and EM-DPA (green) implementations.

REFERENCES

1. S. Manzeli, D. Ovchinnikov, D. Pasquier, O. V. Yazyev, A. Kis, *Nature Reviews Materials* **2**, 1–15 (2017).
2. B. Radisavljevic, A. Radenovic, J. Brivio, V. Giacometti, A. Kis, *Nature nanotechnology* **6**, 147–150 (2011).
3. J. Xu *et al.*, *Science advances* **3**, e1602246 (2017).
4. M. Chhowalla, D. Jena, H. Zhang, *Nature Reviews Materials* **1**, 1–15 (2016).
5. F. Schwierz, J. Pezoldt, R. Granzner, *Nanoscale* **7**, 8261–8283 (2015).
6. F. Xi *et al.*, presented at the 2024 IEEE International Electron Devices Meeting (IEDM), pp. 1–4.
7. G. S. K. César Javier Lockhart de la Rosa, *semiconductor digest* (2024).
8. G. Gaddemane, W. G. Vandenberghe, M. L. Van de Put, E. Chen, M. V. Fischetti, *Journal of Applied Physics* **124** (2018).
9. G. Gaddemane *et al.*, *Physical Review B* **98**, 115416 (2018).
10. Z. Jin, X. Li, J. T. Mullen, K. W. Kim, *Physical Review B* **90**, 045422 (2014).
11. X. Li *et al.*, *Physical Review B* **87**, 115418 (2013).
12. S. Gopalan, S. Mansoori, M. Van de Put, G. Gaddemane, M. Fischetti, *Journal of Computational Electronics* **22**, 1240–1256 (2023).
13. A. Pilotto, P. Khakbaz, P. Palestri, D. Esseni, *Solid-State Electronics* **192**, 108295 (2022).
14. P.-F. Chen, Y.-R. Wu, presented at the 2021 International Symposium on VLSI Technology, Systems and Applications (VLSI-TSA), pp. 1–2.
15. G. Gaddemane, S. Gopalan, M. L. Van de Put, M. V. Fischetti, *Journal of computational electronics* **20**, 49–59 (2021).
16. G. Gaddemane, M. L. Van de Put, W. G. Vandenberghe, E. Chen, M. V. Fischetti, *Journal of Computational Electronics* **20**, 60–69 (2021).
17. J. Backman, Y. Lee, M. Luisier, *Physical Review Applied* **21**, 054017 (2024).
18. G. Gaddemane *et al.*, presented at the 2021 International Conference on Simulation of Semiconductor Processes and Devices (SISPAD), pp. 167–170.
19. R. Duflou, M. Houssa, C. J. L. De La Rosa, G. Kar, A. Afzalian, presented at the 2024 8th IEEE Electron Devices Technology & Manufacturing Conference (EDTM), pp. 1–3.
20. F. Ducry *et al.*, presented at the 2024 8th IEEE Electron Devices Technology & Manufacturing Conference (EDTM), pp. 1–3.
21. P. Giannozzi *et al.*, *Journal of physics: Condensed matter* **21**, 395502 (2009).
22. J.-J. Zhou *et al.*, *Computer Physics Communications* **264**, 107970 (2021).
23. C. Jacoboni, L. Reggiani, *Reviews of modern Physics* **55**, 645 (1983).
24. J. B. Gunn, *Solid State Communications* **1**, 88–91 (1963).